Progress In Electromagnetics Research C, Vol. 123, 151–166, 2022

A Charged Particle Model Based on Weber Electrodynamics for Electron Beam Trajectories in Coil and Solenoid Elements

Christof Baumgärtel and Simon Maher*

Abstract—To aid with the design, evaluation, and optimisation of charged particle instrumentation, computer modelling is often used. It is therefore of interest to obtain accurate predictions for trajectories of charged species with the help of simulation. Particularly for solenoids and coils, which are often used for guiding, deflecting or focussing particle beams, knowledge of the magnetic field is required, especially in the fringing field regions. A novel model, which is based on a direct-line-of-action force between interacting charges, is described in this paper which accurately predicts the deflection of an electron beam trajectory traversing through a coil and the fringe field region. The model is further compared with a standard field model and a commercially available software package. Additionally, a relatively straightforward experiment has been designed and implemented to verify the simulation results, where it is found that the presented direct-action model is equally as accurate as field-based simulations compared with the experimental results. Furthermore, the magnetic field of a solenoid is visualised and analysed in terms of its radial, axial, and total field strength and compared to a force map obtained from the direct-interaction model. This representation allows for further comparison of the field and force interaction models and it is found that they are qualitatively the same.

1. INTRODUCTION

Solenoids and coils are electromagnets which are used to generate magnetic fields of desired strength by supplying a suitable current. A solenoid is defined as an elongated coil of wire whose length is equal to or greater than twice its radius, and most of the field strength is concentrated on the inside of the solenoid. They are common electromagnetic devices which are used in conjunction with many technologies, such as plasma applications [1–5], charged particle optics [6–12], engineering [13–15], and medicine [16–19].

Particularly in charged particle optics, they have become essential elements for guiding and focussing particle beams consisting of protons, ions, or electrons. They are imperative in the functionality of particle accelerators and storage rings, such as the LHC, RHIC, and ELENA. Since the manufacture of these high-tech applications for testing purposes is impractical, it is of interest to obtain accurate simulation of the behaviour of particle beams in the vicinity of electromagnets to aid in the design process of apparatus, so that cost- and time-effectiveness can be ensured. Computer simulation of particle beams is therefore an important tool in the design phase and involves the solution of field equations to obtain information about the electromagnetic field generated by current carrying coils. Numerical methods, such as FEM, FDM and BEM are commonly employed to solve Maxwell's field equations or the Biot-Savart law and the Lorentz force is then used to calculate the action of the field on the beam. Further, the beam can be subject to several disturbing effects, e.g., space charge effects [20–24], which gives further motivation to obtain accurate models of beam trajectories.

Received 15 June 2022, Accepted 16 August 2022, Scheduled 28 August 2022
* Corresponding author: Simon Maher (s.maher@liverpool.ac.uk).
The authors are with the Department of Electrical Engineering and Electronics, University of Liverpool, UK.

As electron beam deflection and the calculation of fields produced by electromagnets is well known, such an arrangement can provide a foundational setup (for experiment and simulation) to test and compare different models of computation. To this end, this paper tests three models for electron beam deflection — a direct-interaction model, a field based model, and predictions obtained with a commercially available software package. We present a direct-interaction model that considers the forces acting between the charge carriers of the electron beam and a coil to predict the deflection experienced by the beam due to the magnetic field, within the low velocity limit $v \ll c$. The standard field model [25] is based on the derivations of Derby & Olbert [26] and Callaghan & Maslen [27], which has been further applied to solenoids with permeable cores, off-axis solenoids, parallel solenoids and axis alignment measurements [28–33]. These two models will be further compared to commercially available software CPO [34].

In order to further test the fidelity of these models, a standard and relatively straightforward experiment is performed where an electron beam travels through a current carrying coil which alters its trajectory. By utilising an initial electrostatic offset it is possible to investigate the deflection experienced by the beam when entering the coil at different angles, i.e., it will propagate through the fringe field region, entering into the inside of the coil where the field is strongest, and its deflection measured on a fluorescent screen at the other end of the coil. Lastly, we will show a visual representation of the magnetic field where the field strength is shown on a two dimensional intensity map and compared with the vectorial force components obtained from the direct-interaction model.

2. MATHEMATICAL MODELLING

This section will present three different models used for predicting the deflection caused by a coil on a beam passing through any field region. First, we will present a direct-action model based on Weber electrodynamics which calculates the force between coil and electron beam without the necessity of field entities $\vec{E}$ & $\vec{B}$. Second, a standard Maxwellian field approach is shown where the fields are calculated first and then substituted into the Lorentz force [25–27]. Third, the software package CPO [34] is used to calculate beam deflections, which employs the BEM to obtain numerical solutions. Recently, research interest in Weber electrodynamics has increased, where Weber's force has not only been applied to electron beam deflection [35–37], but also to other electromagnetic phenomena, such as induction [38–40], and superconductivity [41, 42]. Moreover, the theory has further been connected to the fine structure of the hydrogen atom [43, 44] and even Planck's constant [45, 46]. We will thus show how our model can predict accurate beam trajectories.

2.1. Weber Model

The basis of the present model is given by the direct-action-at-a-distance force for electrodynamic interaction given by Wilhelm Weber in 1846 [47], which was published 15 years prior to Maxwell's first work on electromagnetic vortices [48]. In Maxwell's *Treatise* [49], first published in 1873 where a rigorous treatment of fields and aether was given [50], he even expressed praise for Weber's force law. This electrodynamic force law determines the interaction of charged particles, and in modern vector notation and SI-units is given as:

$$\vec{F}_{21} = \frac{q_1 q_2}{4\pi\varepsilon_0}\frac{\hat{r}_{12}}{r_{12}^2}\left(1 - \frac{\dot{r}_{12}^2}{2c^2} + \frac{r_{12}\ddot{r}_{12}}{c^2}\right). \tag{1}$$

Here, we have $\vec{r_{12}}$ as the relative position, $\dot{r_{12}}$ as the relative velocity, and $\ddot{r_{12}}$ as the relative acceleration between the charges q_1 and q_2, with ε_0 being the permittivity of free space and c the speed of light. We note the relative quantities as

$$\vec{r}_{12} = \vec{r}_1 - \vec{r}_2, \tag{2}$$

$$\dot{r}_{12} = \frac{dr_{12}}{dt} = \hat{r}_{12}\cdot\vec{v}_{12}, \tag{3}$$

$$\ddot{r}_{12} = \frac{d^2 r_{12}}{dt^2} = \frac{d\dot{r}_{12}}{dt} = \frac{[\vec{v}_{12}\cdot\vec{v}_{12} - (\hat{r}_{12}\cdot\vec{v}_{12})^2 + \vec{r}_{12}\cdot\vec{a}_{12}]}{r_{12}}, \tag{4}$$

as well as their magnitude and unit vector

$$r_{12} = |\vec{r}_1 - \vec{r}_2|, \qquad \hat{r}_{12} = \frac{\vec{r}_{12}}{r_{12}}. \tag{5}$$

As Weber's force acts along the line joining the particles it follows Newton's third law, conserving linear momentum, and it further follows conservation of energy and angular momentum. The force reduces to Coulomb's force in the static case for charges at rest, and for the interaction of current elements Ampère's force is derived from it. While it does not conceptually depend on electromagnetic fields, the force has been shown to be consistent with Maxwell's field equations as well [51–55], although as a direct-action formulation such a form of mediation is not needed to transmit the force between charges. Previously, a model has been derived for the deflection of electron beams travelling across current carrying solenoids based on this force approach in earlier work [35, 37]. In this work we present a similar 3D model based on Weber's force. For the first time, this is applied to the electron beam travelling through the current carrying coil with predictions compared to experimental results.

First, we can assume the positions of the electrons in the beam and the current in a coil or solenoid w.r.t. to the coordinate origin, set in the very centre of the coil and obtain the position vectors $\vec{r}_1$, $\vec{r}_2$ and $\vec{r}_{12}$ (see Fig. 1).

$$\vec{r}_1 = \begin{pmatrix} x_1 \\ y_1 \\ z_1 \end{pmatrix}, \quad \vec{r}_2 = \begin{pmatrix} R\cos(\theta) \\ R\sin(\theta) \\ z_2 + dz\theta \end{pmatrix}, \tag{6}$$

$$\vec{r}_{12} = \begin{pmatrix} x_1 - R\cos(\theta) \\ y_1 - R\sin(\theta) \\ z_1 - z_2 - dz\theta \end{pmatrix}, \tag{7}$$

$$r_{12} = \sqrt{(x_1 - R\cos(\theta))^2 + (y_1 - R\sin(\theta))^2 + (z_1 - z_2 - dz\theta)^2}. \tag{8}$$

Here, the initial position of the electron beam is kept arbitrary with the general variables x_1, y_1 , z_1 to allow for any desired point of emission. The current through the coil I is considered as the movement of the electrons in a helical motion along the windings, entering the coil at $z_2 = -l/2$ and moving towards the opposite end with infinitesimal steps of $dz\theta$. In this case, dz acts as a fixed increment which can be obtained from the coil geometry. The motion of the electron beam itself is also kept as general velocity

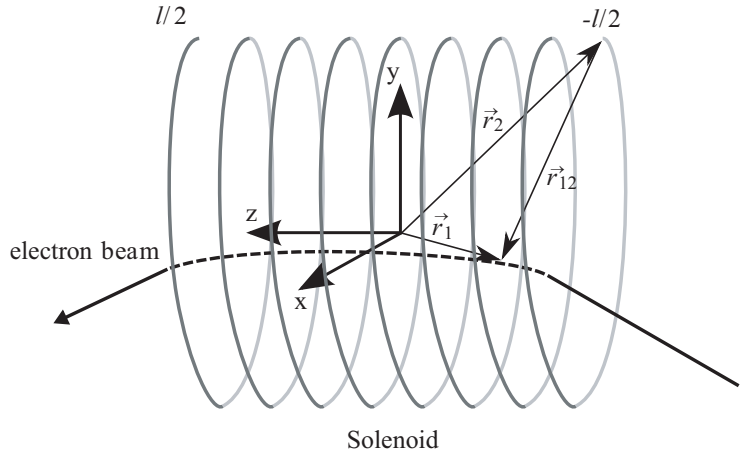

Figure 1. Coordinate system situated in the centre of a solenoid with an electron beam entering at one end and exiting the other. The positions $\vec{r}_1$, $\vec{r}_2$ and $\vec{r}_{12}$ are used to calculate the force on the beam exerted by the current in the coil, elongating from $-l/2$ to $l/2$.

variables $v_{1_x},\ v_{1_y},\ v_{1_z}$, which leads to the velocities

$$\vec{v}_1 = \begin{pmatrix} v_{1_x} \\ v_{1_y} \\ v_{1_z} \end{pmatrix}, \quad \vec{v}_2 = \begin{pmatrix} -v_2\sin(\theta) \\ v_2\cos(\theta) \\ \dfrac{v_2}{R}dz \end{pmatrix}, \quad \vec{v}_{12} = \begin{pmatrix} v_{1_x} + v_2\sin(\theta) \\ v_{1_y} - v_2\cos(\theta) \\ v_{1_z} - \dfrac{v_2}{R}dz \end{pmatrix}. \tag{9}$$

The beam is then set to travel parallel to the axis of the coil by setting the initial value of v_{1_z} equal to the electron velocity v_e and can then enter the coil at an angle by setting initial values for v_{1_x} or v_{1_y}. The initial values are achieved by an electrostatic offset which will be further explained in Section 3.

These velocities and positions can now be substituted into the Weber force (1) to formulate a force $\vec{F}_{2-1-}$between the electrons in the beam q_{1-} and the electrons in the coil q_{2-} and respectively a force $\vec{F}_{2+1-}$ between q_{1-} and the lattice charges q_{2+}. Here we will assume that $q_{1-} = -q_{1+}$ and $q_{2-} = -q_{2+}$.

$$\begin{aligned}
\vec{F}_{2-1-} &= \frac{q_{1+}q_{2+}}{4\pi\varepsilon_0}\frac{\vec{r}_{12}}{r_{12}^3}\left\{1 - \frac{3}{2c^2}\frac{1}{r_{12}^2}\left[\begin{pmatrix} x_1 - R\cos(\theta) \\ y_1 - R\sin(\theta) \\ z_1 - z_2 - dz\theta \end{pmatrix}\cdot\begin{pmatrix} v_{1_x} + v_2\sin(\theta) \\ v_{1_y} - v_2\cos(\theta) \\ v_{1_z} - \dfrac{v_2}{R}dz \end{pmatrix}\right]^2\right. \\
&\qquad \left. + \frac{1}{c^2}\left(\begin{pmatrix} v_{1_x} + v_2\sin(\theta) \\ v_{1_y} - v_2\cos(\theta) \\ v_{1_z} - \dfrac{v_2}{R}dz \end{pmatrix}^2 + \begin{pmatrix} x_1 - R\cos(\theta) \\ y_1 - R\sin(\theta) \\ z_1 - z_2 - dz\theta \end{pmatrix}\cdot\begin{pmatrix} a_{1_x} - a_{2_x} \\ a_{1_y} - a_{2_y} \\ a_{1_z} - a_{2_z} \end{pmatrix}\right)\right\} \\
&= \frac{q_{1+}q_{2+}}{4\pi\varepsilon_0}\frac{\vec{r}_{12}}{r_{12}^3}\left\{1 - \frac{3}{2c^2}\frac{1}{r_{12}^2}\left[(v_{1_x} + v_2\sin(\theta))(x_1 - R\cos(\theta)) + (v_{1_y} - v_2\cos(\theta))(y_1 - R\sin(\theta))\right.\right. \\
&\qquad \left. + \left(v_{1_z} - \frac{v_2}{R}dz\right)(z_1 - z_2 - dz\theta)\right]^2 + \frac{1}{c^2}\left(\left(v_{1_x}^2 + 2v_{1_x}v_2\sin(\theta) + v_2^2\sin^2(\theta)\right.\right. \\
&\qquad + v_{1_y}^2 - 2v_{1_y}v_2\cos(\theta) + v_2^2\cos^2(\theta) + v_{1_z}^2 - 2\frac{v_{1_z}v_2}{R}dz + \left(\frac{v_2}{R}dz\right)^2\Big) \\
&\qquad + (a_{1_x} - a_{2_x})(x_1 - R\cos(\theta)) + (a_{1_y} - a_{2_y})(y_1 - R\sin(\theta)) \\
&\qquad \left.\left. + (a_{1_z} - a_{2_z})(z_1 - z_2 - dz\theta)\right)\right\}
\end{aligned} \tag{10}$$

$$\begin{aligned}
\vec{F}_{2+1-} &= -\frac{q_{1+}q_{2+}}{4\pi\varepsilon_0}\frac{\vec{r}_{12}}{r_{12}^3}\left\{1 - \frac{3}{2c^2}\frac{1}{r_{12}^2}\left[\begin{pmatrix} x_1 - R\cos(\theta) \\ y_1 - R\sin(\theta) \\ z_1 - z_2 - dz\theta \end{pmatrix}\cdot\begin{pmatrix} v_{1_x} - 0 \\ v_{1_y} - 0 \\ v_{1_z} - 0 \end{pmatrix}\right]^2\right. \\
&\qquad \left. + \frac{1}{c^2}\left(\begin{pmatrix} v_{1_x} - 0 \\ v_{1_y} - 0 \\ v_{1_z} - 0 \end{pmatrix}^2 + \begin{pmatrix} x_1 - R\cos(\theta) \\ y_1 - R\sin(\theta) \\ z_1 - z_2 - dz\theta \end{pmatrix}\cdot\begin{pmatrix} a_{1_x} - 0 \\ a_{1_y} - 0 \\ a_{1_z} - 0 \end{pmatrix}\right)\right\} \\
&= -\frac{q_{1+}q_{2+}}{4\pi\varepsilon_0}\frac{\vec{r}_{12}}{r_{12}^3}\left\{1 - \frac{3}{2c^2}\frac{1}{r_{12}^2}\left[(v_{1_x})(x_1 - R\cos(\theta)) + (v_{1_y})(y_1 - R\sin(\theta))\right.\right. \\
&\qquad \left. + (v_{1_z})(z_1 - z_2 - dz\theta)\right]^2 + \frac{1}{c^2}\left(\left(v_{1_x}^2 + v_{1_y}^2 + v_{1_z}^2\right)\right. \\
&\qquad \left.\left. + (a_{1_x})(x_1 - R\cos(\theta)) + (a_{1_y})(y_1 - R\sin(\theta)) + (a_{1_z})(z_1 - z_2 - dz\theta)\right)\right\}
\end{aligned} \tag{11}$$

We can see that acceleration terms $\vec{a}_1$ of the beam cancel out and with the additional assumptions of $v_1 \gg v_2$ and a_2 being negligibly small, we can sum the two forces as

$$\begin{aligned}
\vec{F}_w &= \vec{F}_{2-1-} + \vec{F}_{2+1-} \\
&= \frac{q_{1+}q_{2+}}{4\pi\varepsilon_0}\frac{v_2}{c^2}\frac{\vec{r}_{12}}{r_{12}^3}\left\{-\frac{3}{r_{12}^2}\left[(v_{1_x}\sin(\theta))(x_1 - R\cos(\theta))^2\right.\right. \\
&\qquad \left.\left. + (v_{1_y}\sin(\theta) - v_{1_x}\cos(\theta))(x_1 - R\cos(\theta))(y_1 - R\sin(\theta))\right.\right.
\end{aligned}$$

$$
\begin{aligned}
&- \left(v_{1_y}\cos(\theta)\right)\left(y_1 - R\sin(\theta)\right)^2 + \left(v_{1_z}\sin(\theta) - v_{1_x}\frac{dz}{R}\right)(x_1 - R\cos(\theta))(z_1 - z_2 - dz\theta) \\
&+ \left(-v_{1_z}\cos(\theta) - v_{1_y}\frac{dz}{R}\right)(y_1 - R\sin(\theta))(z_1 - z_2 - dz\theta) \\
&+ \left(-v_{1_z}\frac{dz}{R}\right)(z_1 - z_2 - dz\theta)^2\Big] + \Big[v_{1_x}\sin(\theta) - v_{1_y}\cos(\theta) - \frac{v_{1_z}}{R}dz\Big]\Big\}. \qquad (12)
\end{aligned}
$$

To transition from discrete current sources $q_{1,2}$ to continuous currents, we consider the following assumption: while a continuous current is flowing through the coil, each current element (consisting of a moving electron and a stationary lattice charge) is immediately replaced with the next. This holds a linear charge density λ and we can apply the transformation $qv \to \lambda v\vec{dl} \to IRd\theta$, replacing q_2v_2. When this is integrated over the helical path of the entire coil, the total force exerted on the beam can be evaluated, giving:

$$
\vec{F}_{w_{helix}} = \frac{q_{1+}IR}{4\pi\varepsilon_0 c^2}\int_0^{N2\pi}\left\{\frac{\vec{r}_{12}}{r_{12}^3}\ldots\right\}d\theta. \qquad (13)
$$

Here, N is the total number of windings of the coil. Next to just the helical model, it can also be assumed that the coil consists of individual stacked loops and their action on the beam can be superposed to arrive at a summation approach. In this case $v_{1_z} = 0$ and the infinitesimal dz is replaced with a position for each loop determined by the pitch of the coil $p \cdot (n-1)$, with $n = 1 \ldots N$, so that we have

$$
\vec{r}_2 = \begin{pmatrix} R\cos(\theta) \\ R\sin(\theta) \\ z_2 + p\cdot(n-1)\end{pmatrix}, \quad \vec{v}_2 = \begin{pmatrix} -v_2\sin(\theta) \\ v_2\cos(\theta) \\ 0\end{pmatrix}. \qquad (14)
$$

This can be again substituted into the Weber force with the same assumptions, which then leads to the summation of all individual loops as

$$
\begin{aligned}
\vec{F}_{w_{sum}} = \frac{q_{1+}q_{2+}}{4\pi\varepsilon_0}\frac{v_2}{c^2}\frac{\vec{r}_{12}}{r_{12}^3}\Big\{&-\frac{3}{r_{12}^2}\big[(v_{1_x}\sin(\theta))(x_1 - R\cos(\theta))^2 \\
&+ (v_{1_y}\sin(\theta) - v_{1_x}\cos(\theta))(x_1 - R\cos(\theta))(y_1 - R\sin(\theta)) \\
&- (v_{1_y}\cos(\theta))(y_1 - R\sin(\theta))^2 + v_{1_z}\sin(\theta)(x_1 - R\cos(\theta))(z_1 - z_2 - p(n-1)) \\
&- v_{1_z}\cos(\theta)(y_1 - R\sin(\theta))(z_1 - z_2 - p(n-1))] + [v_{1_x}\sin(\theta) - v_{1_y}\cos(\theta)]\Big\}, \qquad (15)
\end{aligned}
$$

$$
\vec{F}_{w_{sum}} = \frac{q_{1+}IR}{4\pi\varepsilon_0 c^2}\sum_{n=1}^{N}\int_0^{2\pi}\left\{\frac{\vec{r}_{12i}}{r_{12i}^3}\ldots\right\}d\theta. \qquad (16)
$$

Both (13) and (16) can be used to simulate the behaviour of the beam travelling through the coil. The simulation first defines the initial values for $\vec{v}_1$ and $\vec{r}_1$ and then utilises equations of motion to update the positions and velocities for each step. To this end, the propagation of the beam is transitioned from the spatial to the time dimension. The time step is set to be the total distance travelled by an undeflected beam (from emission to detector screen) over the initial electron velocity, so that

$$
\Delta t = \frac{\Delta z_1}{v_e}, \qquad (17)
$$

with $t_0 = 0$ and $t_{last} = z_{1_{last}}/v_e$.

At every time step the force (13) (respectively (16)) is then calculated, and this force will subject the beam to a certain acceleration $\vec{a}_f$. Within the low velocity limit, we can assume the electron mass m_e as constant and obtain $\vec{a}_f$ through the Weber force acting on the beam:

$$
\vec{a}_f = \frac{1}{m_e}\vec{F}_w. \qquad (18)
$$

With this the positions and velocities for the following time step can be calculated according to the equations of motion

$$x_{1_{k+1}} = x_{1_k} + v_{1_{x_k}}\Delta t + \frac{1}{2}a_{f_x}\Delta t^2, \tag{19}$$

$$y_{1_{k+1}} = y_{1_k} + v_{1_{y_k}}\Delta t + \frac{1}{2}a_{f_y}\Delta t^2, \tag{20}$$

$$z_{1_{k+1}} = z_{1_k} + v_{1_{z_k}}\Delta t + \frac{1}{2}a_{f_z}\Delta t^2, \tag{21}$$

$$v_{1_{x_{k+1}}} = v_{1_{x_k}} + a_{f_x}\Delta t, \tag{22}$$

$$v_{1_{y_{k+1}}} = v_{1_{y_k}} + a_{f_y}\Delta t, \tag{23}$$

$$v_{1_{z_{k+1}}} = v_{1_{z_k}} + a_{f_z}\Delta t, \tag{24}$$

where k is an index value denoting the current time step and $k+1$ the following time step. The simulation itself is carried out in *MATLAB* (Mathworks, USA) where the trapezium rule is used to integrate for θ at each time step with a step size of 0.5°. The beam position $\vec{r}_1$ can then be read at the penultimate time step to obtain the horizontal and vertical deflections x_d and y_d respectively, where they are intercepted by the detector screen. Both approaches, helical and summation, predict the same deflection values for a given coil, as expected, and the simulation results are further compared with experiments and the other models in Section 4. Further, it is found that the force component acting longitudinal to the beam (F_{w_z} in this case) is zero, which is in agreement with the Lorentz force.

2.2. Field Model

To calculate the deflections of the beam due to the magnetic field, one needs to obtain the Lorentz force,

$$\vec{F} = q\left(\vec{E} + \vec{v}\times\vec{B}\right), \tag{25}$$

where a charge q is moving at speed $\vec{v}$ and is deflected by the electrical field $\vec{E}$ and the magnetic field $\vec{B}$. In our case, the magnetic field $\vec{B}$ is generated by the current carrying coil and acts on the beam electrons. In order to obtain the magnetic field itself, a useful tool in the form of a *MATLAB* code by Cébron is utilised [25]. This code incorporates the work of Derby and Olbert [26] and Callaghan and Maslen [27] who derived the magnetic field expressions inside and outside of any finite solenoid with help of the Biot-Savart law.

In their model [26], Derby and Olbert obtained formulations for the radial component B_ρ as well as the axial component B_z, where the residual field $B_{res} = \mu_0 n_{unit} I$ is extracted as a factor. (Here, n_{unit} is the number of turns per unit length, giving B_{res} as the idealised uniform field inside a long solenoid.) This expression is modified for radial and axial components through complete elliptic integrals depending on the geometry of the coil, and solving these gives numerical values for the field for any given position inside and outside of the coil or solenoid. They are calculated as follows:

$$B_\rho = \frac{B_{res}}{\pi}\sqrt{\frac{R}{\rho}}\left[\frac{\omega_\pm^2 - 2}{2\omega_\pm}\mathcal{K}(\omega_\pm) + \frac{\mathcal{E}(\omega_\pm)}{\omega_\pm}\right]_-^+, \tag{26}$$

with $\mathcal{K}$ and $\mathcal{E}$ representing complete elliptic integrals of the first and second kind respectively. Here, the + and − signs are used to indicate the upper and lower bounds after integration. We further have geometrical parameters depending on the dimensions of the coil, which are

$$\omega_\pm = \sqrt{\frac{4R\rho}{(R+\rho)^2 + \xi_\pm^2}}, \tag{27}$$

$$\xi_\pm = z \pm L/2 \tag{28}$$

$$\gamma = (R-\rho)/(R+\rho), \tag{29}$$

$$\zeta_{\pm} = \sqrt{\frac{(R-\rho)^2+\xi_{\pm}^2}{(R+\rho)^2+\xi_{\pm}^2}}, \tag{30}$$

$$\chi_{\pm} = \frac{\xi_{\pm}}{\sqrt{(R+\rho)^2+\xi_{\pm}^2}}. \tag{31}$$

The axial field can then be calculated for $\zeta_+ < 1$ as

$$B_z = \frac{B_r}{\pi}\frac{R}{R+\rho}\frac{1}{\gamma+1}\left[\chi_{\pm}\left(\mathcal{K}\left(\sqrt{1-\zeta_{\pm}^2}\right)+\gamma\Pi\left(1-\gamma,\sqrt{1-\zeta_{\pm}^2}\right)\right)\right]_{-}^{+} \tag{32}$$

and for $\zeta_{\pm} \geqslant 1$ as

$$B_z = \frac{B_r}{\pi}\frac{R}{R+\rho}\frac{1}{\gamma(\gamma+1)}\left[\frac{\chi_{\pm}}{\zeta_{\pm}}\left(\gamma\mathcal{K}\left(\sqrt{1-\frac{1}{\zeta_{\pm}^2}}\right)+\Pi\left(1-\frac{1}{\gamma^2},\sqrt{1-\frac{1}{\zeta_{\pm}^2}}\right)\right)\right]_{-}^{+}, \tag{33}$$

where Π is the complete elliptic integral of the third kind, and ρ is the radial coordinate.

To find the deflection values it is considered that the electric field $\vec{E}$ of a coil is negligibly small, so that the Lorentz force reduces to

$$\vec{F}_L = q(\vec{v}_1 \times \vec{B}). \tag{34}$$

The beam is simulated to travel from emission to detector screen in the time domain at constant speed, with the same time step, distance of travel and initial beam position and velocity as the Weber model in the previous section. At each time step the field values of B_ρ and B_z are calculated, and B_ρ transformed to Cartesian coordinates through the following relations

$$B_x = B_\rho \cdot \frac{x_1}{\rho}, \tag{35}$$

$$B_y = B_\rho \cdot \frac{y_1}{\rho}. \tag{36}$$

With these the vector cross product can be performed to obtain the Lorentz force by substituting the field values into the force equation and the resulting acceleration on the beam can be obtained similar to (18), as

$$\vec{a}_f = \frac{1}{m_e}\vec{F}_L. \tag{37}$$

Through this the same equations of motion (19) can be applied to calculate beam position and velocity for every time step. Horizontal deflection x_d and vertical deflection y_d are thus obtained as the positions at the penultimate time step of the simulation.

2.3. Modelling with CPO

Lastly, beam deflections through the coil are also predicted with a state-of-the-art commercially available software package CPO [34]. With this software the coil is modelled as a stack of current loops set along the z-axis following the geometry of the coil. In the software conventional current is considered, thus a current of 1.00 A is supplied to rotate in the mathematically negative sense, which represents positive rotation of the electrons moving through the coil. Like in the previous models, the coil is centred on the origin and the initial parameters, such as position and velocity of the beam, are set in the software. The beam is set to be treated as individual rays of electrons and the direct method is chosen for tracing of the beam, where the beam is travelling over the whole distance from emission to screen at fixed velocity in direction of the z-axis. After travelling from emission through the inside of the coil, the beam is intercepted by a test plane where the detector screen would be, so that the horizontal and vertical deflections x_d and y_d can be read.

3. EXPERIMENTS

An experiment has been performed to obtain deflection values from the magnetic action exerted on the beam by a current carrying coil. The standard experimental arrangement is congruent with the simulations and represents a well-understood test case for the purpose of comparison. The beam is emitted by an electron gun in a Cathode Ray Tube (CRT) and its position recorded on the fluorescent screen of the CRT. A Hameg 203-6 oscilloscope has been disassembled and modified to adapt the CRT for experimentation, with an external cable connecting electron gun and control circuit. A single wound coil with 290 windings has been placed around the glass body of the CRT, with a radius of R =159.5 mm and a length of l =170 mm, which is supplied with a current of 1 A. A sketch of the cross section of this setup can be seen in Fig. 2.

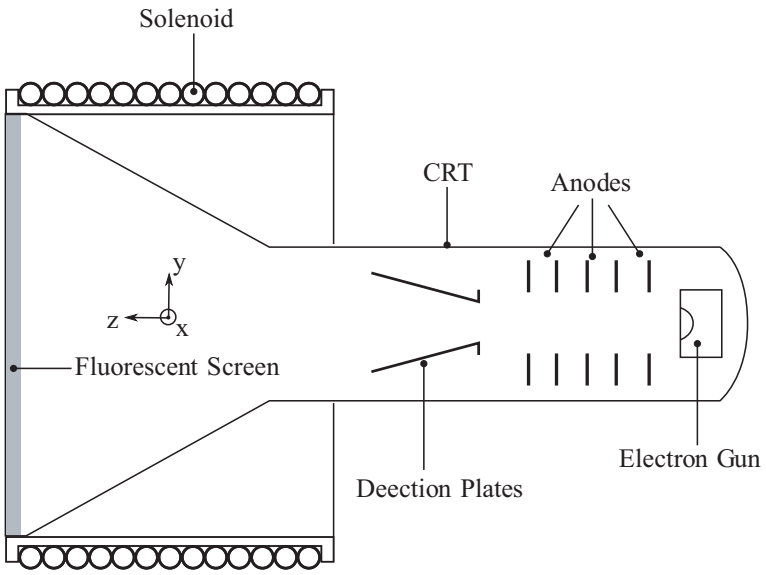

Figure 2. Cross section of the experimental setup comprising a CRT with fluorescent detector screen, surrounded by a coil through which an electron beam is deflected. The electron gun emits the beam, it is accelerated by a set of anodes and then imposed with an initial deflection by the deflection plates to enter the coil at an angle.

With the electron gun operating at an acceleration voltage of 2000 V between cathode and anode, the electrons reach a terminal velocity of

$$v_e = \sqrt{\frac{2eV}{m_e}} \approx 2.65 \times 10^7 \,\mathrm{m\,s^{-1}}. \tag{38}$$

The coil is positioned around the CRT so that the detector screen sits at the end of the coil after the beam has travelled a total distance of 27.5 cm from the point of emission at terminal velocity v_e (38). The electrons are accelerated over a distance of 2.5 cm until they pass the anode and from there travel another 25 cm to the detector screen. The fluorescent screen is factory-equipped with a graticule divided in 10 mm steps and subdivisions of 2 mm, which can give a rough indication of where the beam is intercepted after it has been deflected by the coil. With the control circuit the size of the beam spot can be focused to roughly 1 mm diameter. As the centre of the coil aligns vertically with the point of beam emission (see Fig. 2), the beam is given an initial deflection with the electrostatic deflection plates of the CRT so that it will enter the coil at an angle to the z-axis, which allows one to investigate different magnitudes of deflection. The beam that is initially travelling in a straight line is off-set on the y-axis in steps of 5 mm, which gives the beam an additional velocity component v_{1_y}. Due to the beam travelling a distance of 250 mm after the anode where the vertical deflection plates sit, we obtain a ratio of v_y/v_e in steps of 1/50, reaching from the least initial deflection of 5 mm as 1/50 to 40 mm as 8/50.

These initial deflections, however, necessitate a slight simplification in the simulations so that the deflections can be included through the velocity component v_{1_y} accordingly. It must be assumed here that the beam travels in a straight line from the cathode for the first 25 mm up to the anode and is only deflected by the deflection plates from this point onwards, and respectively not noticeably affected by the magnetic field of the coil up to this point. The closer end of the coil is 80 mm away from the anode and the assumed deflected path of 250 mm is ten times the assumed straight path. It will be seen from the results (in the following section) that this assumption appears reasonable for the present setup and the beam is not significantly deflected by the field for the initial acceleration phase up to the anode.

With this consideration experimental values can be obtained with the following procedure. First the beam is focused and centred in the middle of the graticule on the fluorescent screen. Then it is offset vertically through the deflection plates by the desired amount and lastly the power supply is turned on to deflect the beam with the magnetic field. The vertical and horizontal deflection are both read from the screen with the help of a plastic vernier and the power supply is switched off. This process is repeated five times for each initial deflection value on the y-axis, which allows for obtaining mean values and standard deviations of the experimental data.

4. RESULTS

The observed and predicted deflections in horizontal and vertical directions can be shown as points on the xy-plane and are depicted together in Fig. 3 as a bubble chart. Here horizontal deflection is represented on the axis of abscissae and vertical deflection on the axis of ordinates. The observed data from the experiments is shown as a blue square, and they are directly contrasted with the simulation values in the figure. Results from the Weber model are shown as a red x, field-based values as a yellow triangle and deflections obtained with CPO as a purple circle. Additionally, the data points have different sizes for each of the initial offsets and have been labelled with the ratio of v_y/v_e that initially deflected the beam, so it would enter the coil at different angles, resulting in different deflection values.

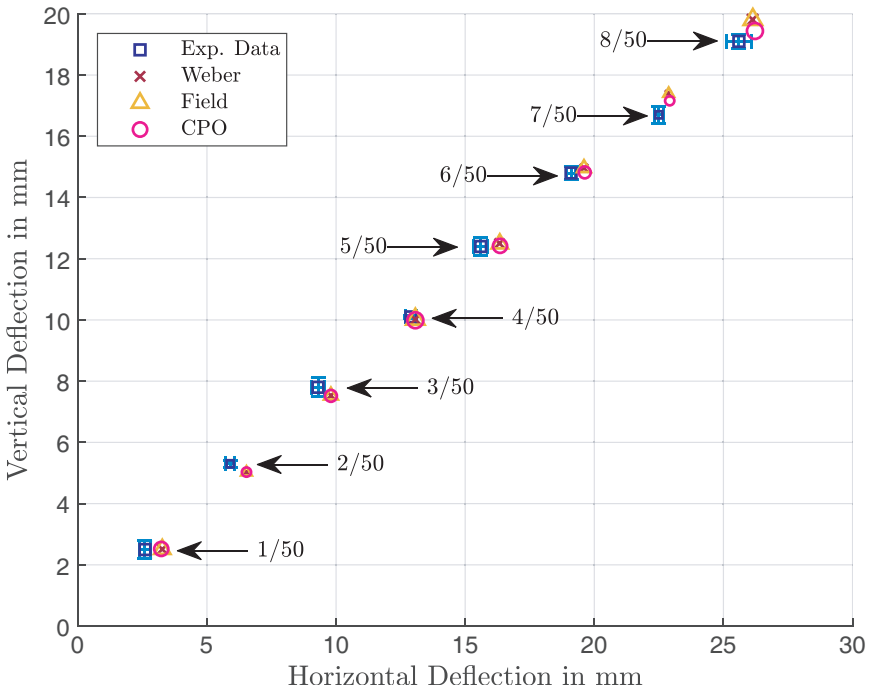

Figure 3. Horizontal and vertical deflections of the beam travelling through a coil with 290 windings. The blue squares represent experimental data, while the red x shows predicted values from the simulations with the Weber force, the yellow triangle predictions with field theory and the purple circle simulation results from CPO. Each data point is labelled with the respective ratio of v_y/v_e.

From this figure we can see that the deflection values follow a trend of increasing vertical and horizontal deflection that seems to grow linearly for stronger initial offset values. The deflection through the magnetic field is minimal for a vertical velocity of 1/50 of the electron velocity, but greatest for the maximum offset value of 8/50 utilised in this experiment. Further, the vertical deflection value y_d can be seen to be nearly half of the initial offset value in mm. The predictions of the three models all follow the overall trend equally well, and they are additionally presented in Table 1, where numerical values from the simulations can be readily compared with the observed experimental data.

Table 1. Deflection results for an electron beam traversing through the 290 turn coil showing simulation results for Weber, field and CPO models next to the observed data acquired from experiment.

v_y/v_e	Weber		Field		CPO		Observed	
	x_d	y_d	x_d	y_d	x_d	y_d	x_d	y_d
1/50	3.27	2.51	3.27	2.51	3.23	2.52	2.6 (±0.28)	2.5 (±0.23)
2/50	6.53	5.02	6.53	5.02	6.53	5.03	5.9 (±0.12)	5.3 (±0.18)
3/50	9.80	7.53	9.80	7.53	9.80	7.52	9.3 (±0.31)	7.8 (±0.25)
4/50	13.07	10.02	13.07	10.02	13.07	9.99	12.9 (±0.04)	10.1 (±0.20)
5/50	16.33	12.50	16.34	12.49	16.35	12.42	15.6 (±0.30)	12.4 (±0.27)
6/50	19.60	14.96	19.60	14.96	19.63	14.82	19.1 (±0.23)	14.8 (±0.18)
7/50	22.86	17.40	22.88	17.39	22.92	17.16	22.5 (±0.27)	16.7 (±0.19)
8/50	26.13	19.81	26.14	19.81	26.22	19.44	25.6 (±0.23)	19.1 (±0.48)

From this table and Fig. 3 it is clear that all three models, CPO, field and Weber give the same deflection results and agree well with experimental measurements for this setup. For the biggest offsets 7/50 and 8/50 Weber and field model seem to marginally overestimate the deflection compared to CPO which is very slightly closer to experimental values in these two cases, but with a difference of only about half a millimetre the values are still almost virtually the same.

Further to the 290 turn coil where experimental values have been obtained, a short coil with 20 turns was additionally simulated to check the behaviour of the beam when travelling through an inhomogeneous field. The hypothetical coil has a radius of 52 mm, length 10 mm and is sitting 100 mm away from the emitting electron gun and 75 mm from the anode respectively, with the coordinate system still considered in the centre of the electromagnet. With a current of 1 A and the same offset values for v_y/v_e simulation results are obtained in exactly the same way as described in Section 2 of this paper, the results of which are presented in the following Table 2.

It appears from these results that, even though the coil is relatively short with only 20 windings and producing a rather inhomogeneous field, there is barely any noticeable deflection on the beam. As

Table 2. Predicted vertical and horizontal deflections for an electron beam traversing through a 20 turn coil where only simulation results are presented for Weber, field and CPO model.

v_y/v_e	Weber		Field		CPO	
	x_d	y_d	x_d	y_d	x_d	y_d
1/50	0.39	4.87	0.39	4.87	0.39	4.87
2/50	0.78	9.73	0.78	9.73	0.78	9.73
3/50	1.17	14.60	1.17	14.60	1.17	14.60
4/50	1.56	19.46	1.56	19.46	1.57	19.46
5/50	1.95	24.33	1.95	24.33	1.96	24.32
6/50	2.34	29.19	2.34	29.19	2.35	29.19
7/50	2.72	34.05	2.73	34.05	2.75	34.05
8/50	3.11	38.91	3.11	38.91	3.15	38.90

the v_y/v_e ratios correspond to initial offsets in 5 mm steps, the beam is almost not shifted from the vertical y-offset at all. Further, only an ever so slight displacement is predicted for the position on the x-axis, so overall the electron beam is barely shifted at all. Nevertheless, all three models predict very similar deflection values and are in good agreement with each other.

5. FURTHER ANALYSIS OF THE MAGNETIC FIELD

Upon demonstrating the similarity of the electron deflection results with Weber's force and field theory alike, it appears feasible to analyse the field itself further. It has been argued by Slepian [56] that lines of force do not need to be continuous, individual or closed curves and that it is enough to know only the local vectorial value of the field in direction and magnitude to predict observable phenomena. In this sense, the field can be thought of as a vectorial map that indicates how much interaction of charged particles is possible in which direction at any point in space. It is possible to compare this with Weber's theory directly if we obtain a similar map of the force values like the map of the field values.

The total magnetic field of a given solenoid at any point can be expressed as $B = \sqrt{B_\rho^2 + B_z^2}$ which gives the magnitude of the vectorial components. A similar expression can be obtained with the Weber force. With the electrons at 2000 eV, the force values in the yz-plane can be calculated, where $x = 0$ and $\rho = y$ with the electrons moving in x-direction, in order to give a cross section of a solenoid's field in the ρz-plane. In order to compare this with the total field values B, the total force is similarly obtained as

$$F_w = \sqrt{F_x^2 + F_y^2 + F_z^2} \tag{39}$$

and can then be scaled by the electron velocity to the total field values according to

$$B_w = \frac{F_w}{q v_e}. \tag{40}$$

Here, B_w can be interpreted as the magnitude of total "force-field" values based on Weber's force. It must be noted that this is not a strict equivalence since only the magnitudes have been manipulated and this does not apply in the same way to the vectorial values themselves, as the Lorentz force is based on a cross product. Nevertheless, for the magnitudes we can now see that B_w is also in units of T and a comparison of the field and the Weber force becomes possible.

These calculations have been carried out for a solenoid of 255 mm length, 27 mm radius, and 560 turns. The field and force values were simulated to an accuracy of 1 mm for both z- and ρ-axis and in Fig. 4(a) we can see the total field B from the Derby & Olbert model and the values for B_w are shown next to it in Fig. 4(b). The white lines in the Figure are situated at $\rho = \pm R$ and their value is undefined. This is due to the definition of γ (29), which will inevitably lead to a division by zero problem and the algorithm did not converge in this case.

As can be seen from this juxtaposition, both field and Weber force represented by these magnitudes are exactly the same, qualitatively as well as quantitatively. The black lines represent the dimension of the solenoid and it can be seen that most interaction is possible inside of the solenoid, where the field is strongest. Anywhere outside of the solenoid (except very close to the ends) the field values are much smaller than inside. As expected, it can also be seen that the field outside has a tendency to concentrate closer to the poles and falls off with increasing distance, which seems consistent with the notion that an ideal, infinitely long solenoid only produces a field inside of itself and does not have a field outside. (Note: Since the field values outside the solenoid are one or two orders of magnitude smaller than the strong values inside the solenoid, the shades of blue might be difficult to distinguish in printed version. However, their structure can be better seen in the digital version.)

Further to the comparison of the total field values, we can also analyse the individual components of the field and the force respectively. Since the values for both field and force have been obtained in the yz-plane, we find that $F_x = 0$, $B_x = 0$ and of course $B_\rho = B_y$. This way we can compare the axial field values B_z (Fig. 5(a)) with the vertical force values F_y (Fig. 5(b)) and the radial field values B_ρ (Fig. 6(a)) to the horizontal force values F_z (Fig. 6(b)). However, in this case, we cannot apply a scaling factor for the vectorial values, so only a qualitative comparison is possible. Nonetheless, it is instructive to look at the magnitudes of the respective field and force components. (Since the direction

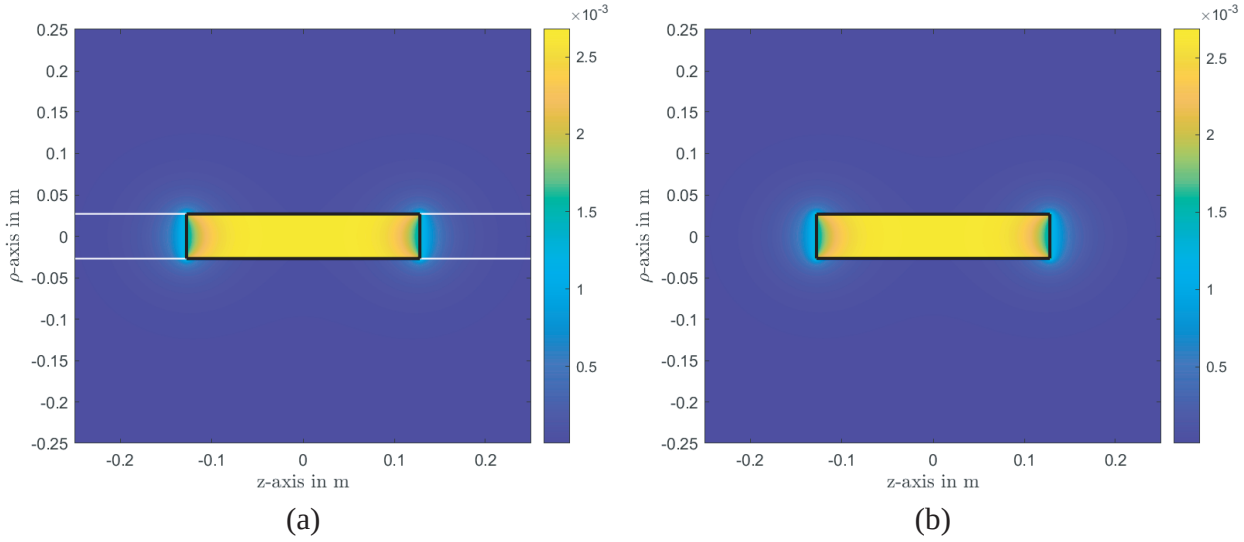

Figure 4. A comparison of the magnitude of field $\vec{B}$ as produced by a solenoid in the ρz-plane with the magnitude of Weber force scaled to a 'force field' representation $\vec{B_w}$, both in units of T; (a) field magnitudes calculated with the model by Derby & Olbert and respective code [25]; (b) representation of the Weber force as a field magnitude scaled by charge q and electron velocity v_e according to Equation (40).

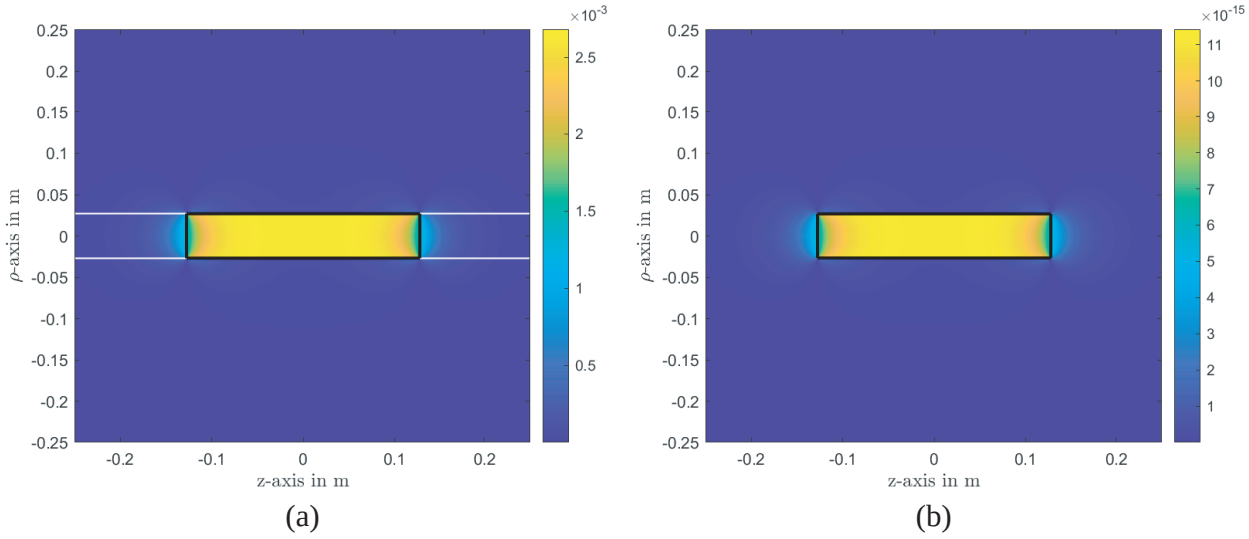

Figure 5. Direct comparison of individual components of field and force values, represented by their magnitude in the ρz-plane; (a) axial field component B_z; (b) vertical Weber force component F_y.

of the field, respectively force, changes inside and outside of the solenoid, it is advantageous to look at just the magnitudes again, as it allows for easier comparison of the values.)

Even though the magnitude of the force is much smaller than the field value (as the field is in units of T while the force is in N, of course,) it is easy to see that they are qualitatively the same, i.e., B_z and F_y are similar and so are B_ρ and F_z. These relations are hardly surprising as we have seen in the previous section that the deflection values are similar, so the field and force values must be similar too. Furthermore, it can be seen that the axial field is primarily responsible for the strong field inside of the solenoid and also contributes to the field outside of the solenoid and close to the poles. The radial field is mostly only contributing to field values around the poles themselves, which suggests that the radial field component has a notable influence in the fringe field region.

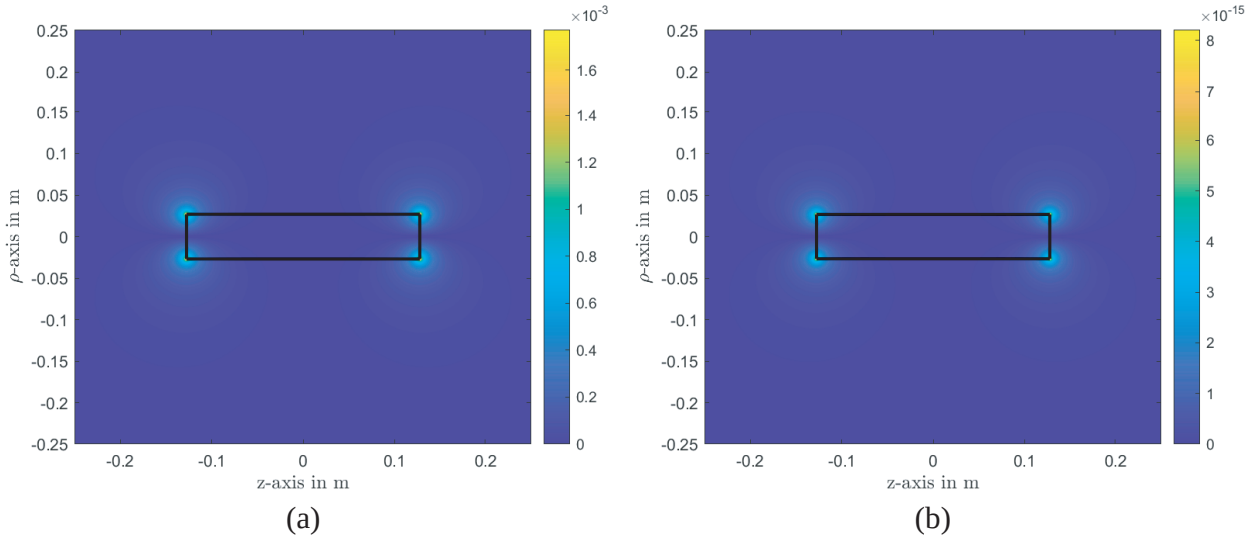

Figure 6. Direct comparison of individual components of field and force values, represented by their magnitude in the ρz-plane; (a) radial field component B_ρ; (b) horizontal Weber force component F_z.

6. CONCLUSION

This paper has investigated the suitability of a particle-based model (derived from Weber electrodynamics) to predict experimental electron beam deflections in a standard configuration, as compared against a standard field-based model and a commercial software package (also field-based). The experimental setup consisted of a low velocity electron beam (2000 eV) travelling through a 290 turn coil. The deflection caused by the electromagnet has been simulated with three different models, two field based models and a direct-action model based on Weber electrodynamics. It was found that the three models agree well with experimental data and predict similar deflection values, where they were found to be equally accurate. Furthermore, the magnetic field of a solenoid was visually analysed in a plane and compared with a "force field" description obtained from Weber electrodynamics. They were found to be the same qualitatively and moreover, after algebraic manipulation, also quantitatively. This is in agreement with the models predicting approximately equal deflection values for the simulated electron beam. As Weber's force has been shown to be consistent with field equations and Lorentz force before, this is not a particularly surprising result, and the theories appear to be indistinguishable in the near field and low velocity limit. However, Weber's force follows energy and momentum conservation and the direct-action model presented here can directly calculate the force between beam and electromagnet without needing the field as a mediator. This could be advantageous in certain situations where complicated geometrical structures are utilised, as any geometry can potentially be implemented. Since the present model is limited to the low velocity regime, it could be of interest for particle decelerators and storage rings where low energy beams are utilised. Further, the Weber model presented here is is foundational, and demonstrates its applicability for this relatively straightforward test case. This can likely be adapted and advanced in the future for more complex beam focussing arrangements, or to take into account space charge effects from particle-particle interactions through superposition of forces or statistical treatment of charges (e.g., by utilising the virial theorem [57]). Other disturbing effects, such as tune shifts or chromaticity shifts could be incorporated into a particle-based model.

ACKNOWLEDGMENT

One of the authors (CB) is funded by the School of Electrical Engineering, Electronics and Computer Science (EEE-CS), University of Liverpool. CB and SM are thankful to the EEE-CS School in this regard. The Authors would like to acknowledge assistance from J. Gillmore at the University of Liverpool for his assistance in modifying the electronics for the electron gun and to Prof. F. Read

for his assistance with the CPO software package. The authors would also like to thank Dr. R. T. Smith for fruitful discussions.

REFERENCES

1. Steinhauer, L. and D. Quimby, "Advances in laser solenoid fusion reactor design," *The Technology of Controlled Nuclear Fusion: Proceedings of the Third Topical Meeting on the Technology of Controlled Nuclear Fusion*, Vol. 1, 121, National Technical Information Service, Santa Fe, New Mexico, May 9–11, 1978.
2. Tobita, K., S. Nishio, M. Sato, S. Sakurai, T. Hayashi, Y. Shibama, T. Isono, M. Enoeda, H. Nakamura, S. Sato, et al., "Slimcs-compact low aspect ratio demo reactor with reducedsize central solenoid," *Nuclear Fusion*, Vol. 47, No. 8, 892, 2007.
3. Engström, C., T. Berlind, J. Birch, L. Hultman, I. Ivanov, S. Kirkpatrick, and S. Rohde, "Design, plasma studies, and ion assisted thin film growth in an unbalanced dual target magnetron sputtering system with a solenoid coil," *Vacuum*, Vol. 56, No. 2, 107–113, 2000.
4. Zhang, X., J. Xiao, Z. Pei, J. Gong, and C. Sun, "Influence of the external solenoid coil arrangement and excitation mode on plasma characteristics and target utilization in a dc-planar magnetron sputtering system," *Journal of Vacuum Science & Technology A: Vacuum, Surfaces, and Films*, Vol. 25, No. 2, 209–214, 2007.
5. Karino, T., M. Okamura, T. Kanesue, S. Ikeda, and S. Kawata, "Plasma instability inside solenoid with laser ion source," *Review of Scientific Instruments*, Vol. 91, No. 5, 053303, 2020.
6. Schröder, G., "Fast pulsed magnet systems," *Handbook of Accelerator Physics and Engineering*, A. W. Chao and M. Tigner, eds., No. CERN-SL-98-017-BT, Ch. 3, 460–466, World Scientific, Singapore, 1999.
7. Wong, L. J., K.-H. Hong, S. Carbajo, A. Fallahi, P. Piot, M. Soljačić, J. D. Joannopoulos, F. X. Kärtner, and I. Kaminer, "Laser-induced linear-field particle acceleration in free space," *Scientific Reports*, Vol. 7, No. 1, 11159, 2017.
8. Arnaudon, L., P. Baudrenghien, C. Bertone, Y. Body, J. Broere, O. Brunner, M. Buzio, C. Carli, F. Caspers, J. Corso, J. Coupard, A. Dallocchio, N. Dos Santos, R. Garoby, F. Gerigk, L. Hammouti, K. Hanke, M. Jones, I. Kozsar, J. Lettry, J. Lallement, A. Lombardi, L. Lopez-Hernandez, C. Maglioni, S. Mathot, S. Maury, B. Mikulec, D. Nisbet, C. Noels, M. Paoluzzi, B. Puccio, U. Raich, S. Ramberger, C. Rossi, N. Schwerg, R. Scrivens, G. Vandoni, S. Weisz, J. Vollaire, M. Vretenar, and T. Zickler, "The LINAC4 Project at CERN," 4, Aug. 2011.
9. Dattoli, G., L. Mezi, and M. Migliorati, "Operational methods for integro-differential equations and applications to problems in particle accelerator physics," *Taiwanese Journal of Mathematics*, 407–413, 2007.
10. Karamyshev, O., C. Welsch, and D. Newton, "Optimization of low energy electrostatic beam lines," *Proceedings of IPAC2014*, 2014.
11. Papash, A., A. Smirnov, and C. Welsch, "Nonlinear and long-term beam dynamics in low energy storage rings," *Physical Review Special Topics — Accelerators and Beams*, Vol. 16, No. 6, 060101, 2013.
12. Maher, S., F. P. Jjunju, and S. Taylor, "Colloquium: 100 years of mass spectrometry: Perspectives and future trends," *Reviews of Modern Physics*, Vol. 87, No. 1, 113, 2015.
13. Taminger, K. M., W. H. Hofmeister, and R. A. Halfey, "Use of beam deflection to control an electron beam wire deposition process," US Patent 8,344,281, Jan. 2013.
14. Koleva, E., V. Dzharov, V. Gerasimov, K. Tsvetkov, and G. Mladenov, "Electron beam deflection control system of a welding and surface modification installation," *Journal of Physics: Conference Series*, Vol. 992, 012013, IOP Publishing, 2018.
15. Kasisomayajula, V., M. Booty, A. Fiory, and N. Ravindra, "Magnetic field assisted heterogeneous device assembly," *Supplemental Proceedings: Materials Processing and Interfaces*, Vol. 1, 651–661, 2012.

16. Fernández-Morán, H., "Electron microscopy with high-field superconducting solenoid lenses," *Proceedings of the National Academy of Sciences of the United States of America*, Vol. 53, No. 2, 445, 1965.
17. Fernández-Morán, H., "High-resolution electron microscopy with superconducting lenses at liquid helium temperatures," *Proceedings of the National Academy of Sciences of the United States of America*, Vol. 56, No. 3, 801, 1966.
18. Bordelon, D. E., R. C. Goldstein, V. S. Nemkov, A. Kumar, J. K. Jackowski, T. L. De-Weese, and R. Ivkov, "Modified solenoid coil that efficiently produces high amplitude ac magnetic fields with enhanced uniformity for biomedical applications," *IEEE Transactions on Magnetics*, Vol. 48, No. 1, 47–52, 2011.
19. Drees, J. and H. Piel, "Particle beam treatment system with solenoid magnets," US Patent App. 15/203,966, Jan. 12 2017.
20. Berz, M., B. Erdélyi, and K. Makino, "Fringe field effects in small rings of large acceptance," *Physical Review Special Topics — Accelerators and Beams*, Vol. 3, No. 12, 124001, 2000.
21. Makino, K. and M. Berz, "Solenoid elements in cosy infinity," *Institute of Physics CS*, Vol. 175, 219–228, 2004.
22. Aslaninejad, M., C. Bontoiu, J. Pasternak, J. Pozimski, and A. Bogacz, "Solenoid fringe field effects for the neutrino factory linac-mad-x investigation," *Tech. Rep.*, Thomas Jefferson National Accelerator Facility, Newport News, VA (United States), 2010.
23. Gorlov, T. and J. Holmes, "Fringe field effect of solenoids," *9th International Particle Accelerator Conference (IPAC2018), IPAC*, 3385–3387, JaCoW Publishing, Vancouver, BC, Canada, 2018.
24. Migliorati, M. and G. Dattoli, "Transport matrix of a solenoid with linear fringe field," *Il Nuovo Cimento della Società Italiana di Fisica-B: General Physics, Relativity, Astronomy and Mathematical Physics and Methods*, Vol. 124, No. 4, 385, 2009.
25. Cebron, D., "Magnetic fields of solenoids and magnets," https://www.mathworks.com/matlabcentral/fileexchange/71881-magnetic-fields-of-solenoids-and-magnets, 2019, Retrieved Sept. 26, 2019.
26. Derby, N. and S. Olbert, "Cylindrical magnets and ideal solenoids," *American Journal of Physics*, Vol. 78, No. 3, 229–235, 2010.
27. Callaghan, E. E. and S. H. Maslen, "The magnetic field of a finite solenoid," *Tech. Rep.*, NASA, 1960.
28. Lerner, L., "Magnetic field of a finite solenoid with a linear permeable core," *American Journal of Physics*, Vol. 79, No. 10, 1030–1035, 2011.
29. Muniz, S. R., V. S. Bagnato, and M. Bhattacharya, "Analysis of off-axis solenoid fields using the magnetic scalar potential: An application to a zeeman-slower for cold atoms," *American Journal of Physics*, Vol. 83, No. 6, 513–517, 2015.
30. Lim, M. X. and H. Greenside, "The external magnetic field created by the superposition of identical parallel finite solenoids," *American Journal of Physics*, Vol. 84, No. 8, 606–615, 2016.
31. Arpaia, P., B. Celano, L. De Vito, A. Esposito, A. Parrella, and A. Vannozzi, "Measuring the magnetic axis alignment during solenoids working," *Scientific Reports*, Vol. 8, No. 1, 11426, 2018.
32. Arpaia, P., L. De Vito, A. Esposito, A. Parrella, and A. Vannozzi, "On-field monitoring of the magnetic axis misalignment in multi-coils solenoids," *Journal of Instrumentation*, Vol. 13, No. 08, P08017, 2018.
33. Arpaia, P., B. Celano, L. De Vito, A. Esposito, N. Moccaldi, and A. Parrella, "Monitoring the magnetic axis misalignment in axially-symmetric magnets," *2018 IEEE International Instrumentation and Measurement Technology Conference (I2MTC)*, 1–6, IEEE, 2018.
34. Read, F. H. and N. J. Bowring, "The cpo programs and the bem for charged particle optics," *Nuclear Instruments and Methods in Physics Research Section A: Accelerators, Spectrometers, Detectors and Associated Equipment*, Vol. 645, No. 1, 273–277, 2011.

35. Smith, R. T., F. P. Jjunju, and S. Maher, "Evaluation of electron beam deflections across a solenoid using Weber-Ritz and Maxwell-Lorentz electrodynamics," *Progress In Electromagnetics Research*, Vol. 151, 83–93, 2015.
36. Smith, R. T. and S. Maher, "Investigating electron beam deflections by a long straight wire carrying a constant current using direct action, emission-based and field theory approaches of electrodynamics," *Progress In Electromagnetics Research B*, Vol. 75, 79–89, 2017.
37. Baumgärtel, C., R. T. Smith, and S. Maher, "Accurately predicting electron beam deflections in fringing fields of a solenoid," *Scientific Reports*, Vol. 10, No. 1, 1–13, 2020.
38. Smith, R. T., S. Taylor, and S. Maher, "Modelling electromagnetic induction via accelerated electron motion," *Canadian Journal of Physics*, Vol. 93, No. 7, 802–806, 2014.
39. Smith, R. T., F. P. Jjunju, I. S. Young, S. Taylor, and S. Maher, "A physical model for low-frequency electromagnetic induction in the near field based on direct interaction between transmitter and receiver electrons," *Proceedings of the Royal Society A: Mathematical, Physical and Engineering Sciences*, Vol. 472, No. 2191, 20160338, 2016.
40. Baumgärtel, C. and S. Maher, "A novel model of unipolar induction phenomena based on direct interaction between conductor charges," *Progress In Electromagnetics Research*, Vol. 171, 123–135, 2021.
41. Assis, A. and M. Tajmar, "Superconductivity with weber's electrodynamics: The london moment and the meissner effect," *Annales de la Fondation Louis de Broglie*, Vol. 42, 307, 2017.
42. Prytz, K. A., "Meissner effect in classical physics," *Progress In Electromagnetics Research M*, Vol. 64, 1–7, 2018.
43. Torres-Silva, H., J. López-Bonilla, R. López-Vázquez, and J. Rivera-Rebolledo, "Weber's electrodynamics for the hydrogen atom," *Indonesian Journal of Applied Physics*, Vol. 5, No. 01, 39–46, 2015.
44. Frauenfelder, U. and J. Weber, "The fine structure of Weber's hydrogen atom: Bohr-sommerfeld approach," *Zeitschrift für angewandte Mathematik und Physik*, Vol. 70, No. 4, 105, 2019.
45. Tajmar, M., "Derivation of the planck and fine-structure constant from Assis's gravity model," *Journal of Advanced Physics*, Vol. 4, No. 3, 219–221, 2015.
46. Baumgärtel, C. and M. Tajmar, "The planck constant and the origin of mass due to a higher order casimir effect," *Journal of Advanced Physics*, Vol. 7, No. 1, 135–140, 2018.
47. Weber, W. E., *Wilhelm Weber's Werke*, Vol. 3 (First part), Julius Springer, Berlin, 1893.
48. Maxwell, J. C., "Xxv. on physical lines of force: Part i. — The theory of molecular vortices applied to magnetic phenomena," *The London, Edinburgh, and Dublin Philosophical Magazine and Journal of Science*, Vol. 21, No. 139, 161–175, 1861.
49. Maxwell, J. C., *A Treatise on Electricity and Magnetism Unabridged*, Dover, 1954.
50. Yaghjian, A., "Reflections on Maxwell's treatise," *Progress In Electromagnetics Research*, Vol. 149, 217–249, 2014.
51. Assis, A. K. T., *Weber's Electrodynamics*, 47–77, Springer, Dordrecht, 1994.
52. Kinzer, E. and J. Fukai, "Weber's force and Maxwell's equations," *Foundations of Physics Letters*, Vol. 9, No. 5, 457–461, 1996.
53. O'Rahilly, A., *Electromagnetic Theory: A Critical Examination of Fundamentals*, Vol. I and II, Dover Publications, 1965.
54. Wesley, J. P., "Weber electrodynamics, Part I. General theory, steady current effects," *Foundations of Physics Letters*, Vol. 3, No. 5, 443–469, 1990.
55. Li, Q., "Electric field theory based on Weber's electrodynamics," *International Journal of Magnetics and Electromagnetism*, Vol. 7:039, No. 2, 1–6, 2021.
56. Slepian, J., "Lines of force in electric and magnetic fields," *American Journal of Physics*, Vol. 19, No. 2, 87–90, 1951.
57. Mendes, R., L. Malacarne, and A. Assis, *Virial Theorem For Weber's Law*, 67–70, Rinton Press, Paramus, 2004.